Case Study

Corrosion analysis of modern and historic railway track with optical, electron and correlative Raman microscopy

ZEISS

Seeing beyond

Authors: Dr. Roger Barnett
Carl Zeiss Microscopy Ltd.

Dr. Ute Schmidt
WITec Wissenschaftliche Instrumente und Technologie GmbH

Date: December 2019

Introduction

Railways and the rail industry are important parts of the infrastructure of most developed countries, being essential for the efficient transport of passengers and freight cross-country and between countries. It is estimated that the UK rail industry contributes £36 billion [1] to the UK economy every year with every aspect of the network requiring regular replacement, maintenance or inspection over its lifetime.

Railway tracks are standard long steel products produced by hot rolling and continuous cooling from the austenitic state. The track profile/cross-section has evolved over time but can be broadly divided into two main types – flat-bottomed rail, which rests directly on railway sleepers, and bullhead rail, which sits in rail chairs that are then attached to the sleeper. Bullhead rail has been almost entirely phased out in the UK since the 1950s in favor of flat-bottomed rail but is still used in some areas and thus produced and sold in small quantities.

Rail track sections are made in massive quantities by many steel companies across the world, including but not limited to Arcelor Mittal, Tata Steel, and Nippon Steel. As train technology has evolved and passenger numbers have increased over the last 100 years, the track undergoes an increasingly harsh environment. Rail track metallurgy and cross-sectional profile have thus evolved to meet these needs. The steel used typically contains high concentrations of carbon (0.4 - 0.8%) with some super premium steels reaching 0.9%.[2] Historically, railway steel has always had a fully pearlitic structure though some modern high-grade railway steels may have a bainitic structure. The microstructure is engineered to have high hardness/wear resistance and resists damage types typical in this service such as rolling contact fatigue. However, these must be balanced against other factors such as cost, weldability and ease of heat treatment.

Case Study

Three samples of railway track were supplied (courtesy of Nene Valley Heritage Railway) and an investigation was carried out to compare the extent of damage to the track structure. This included both mechanical and corrosion damage, as well as as differences in metallurgy and microstructure between the tracks, to better understand degradation and behavior in service.

The track age could be estimated from rail type as well as the cradles in which the rail track had been stored. Some uncertainty remained due to the significant age of the track and possible track-re-use over the last 90 years. Little or no information was available on service history. The track samples are summarized in Table 1 and shown in Figure 1.

Sample A (2017 rail, unused) appears relatively intact, with no visible deformation, but with corrosion of the outer surface. For Samples B and C (1940s-1950s and 1928-1932 rail respectively, both used), removal of material on the top surface was apparent, with deformation visible on the inside corners of the rail. Corrosion and associated corrosion scale were visible on all surfaces; the white layer on the exterior of B and some of C was believed to be a paint or other coating.

Track Sample	Track Profile	Sample Information
A	113A non-prime rail	Single piece. Rolled in 2017, unused
B	95lb bullhead rail	Single piece, used. Believed to be 1940s-1950s. Some surface damage.
C	85lb bullhead rail	4 x pieces from same batch, used. Believed to be 1928-1932.

Table 1 *Samples of railway track, courtesy of Nene Valley Heritage Railway.*
Due to the age of the material plus track reuse over time, exact age of rail cannot be established.

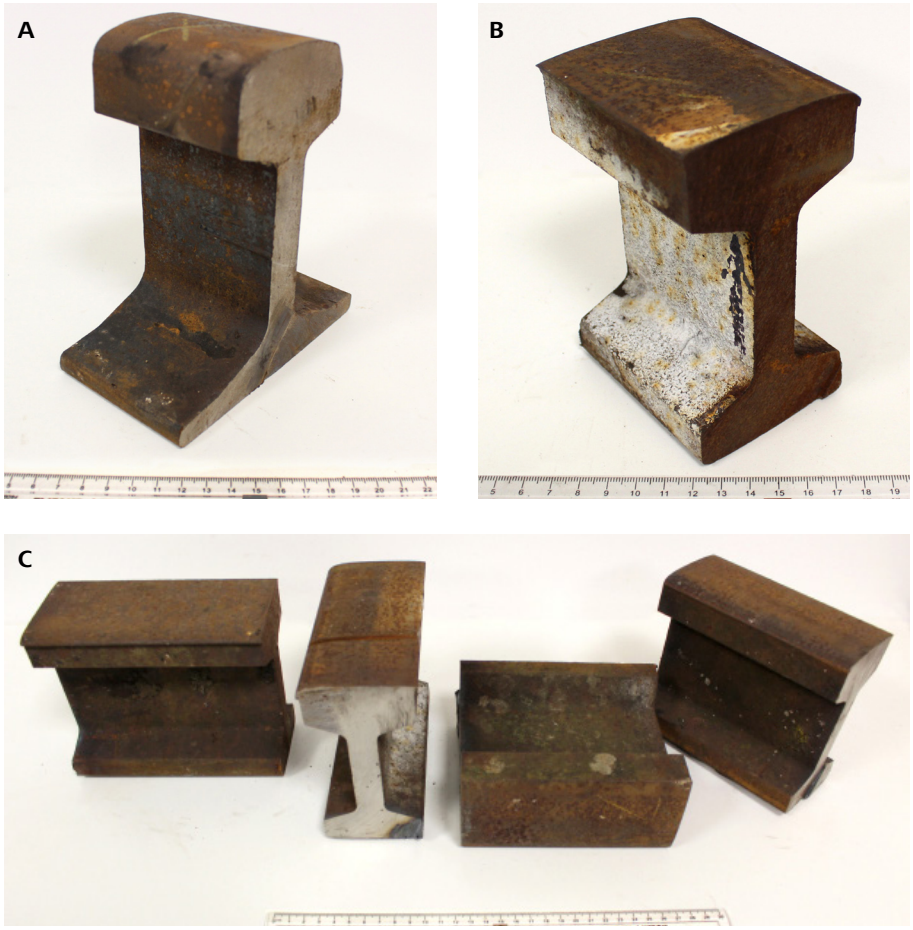

Figure 1 *Railway track samples, courtesy of Nene Valley Heritage Railway – A) 113A non-prime rail, 2017, unused; B) 95 lb bullhead rail, 1940s-1950s, used; C) 85 lb bullhead rail, 1928-1932, unused*

Macro Cross-sectional Analysis

A series of large cross-sections were prepared from the head of each of Sample A and B, plus an example rail from Sample C. These pieces were mounted in non-conductive resin then polished to a 0.25 µm finish and etched to reveal the microstructure (1% Nital solution), Figure 2. An additional 40 mm diameter cross-section was prepared of the upper surface of each rail head. These were mounted in conductive resin and were unetched to facilitate easy scanning electron microscopy.

For both Sample B and Sample C, damage is clearly visible, with the right side of the rail deformed and folded over onto itself, while the left side had a corresponding protrusion.

The cores of Samples B and C also show a clearly different microstructure to the exterior. The same effect can be seen in Sample A but is less pronounced.

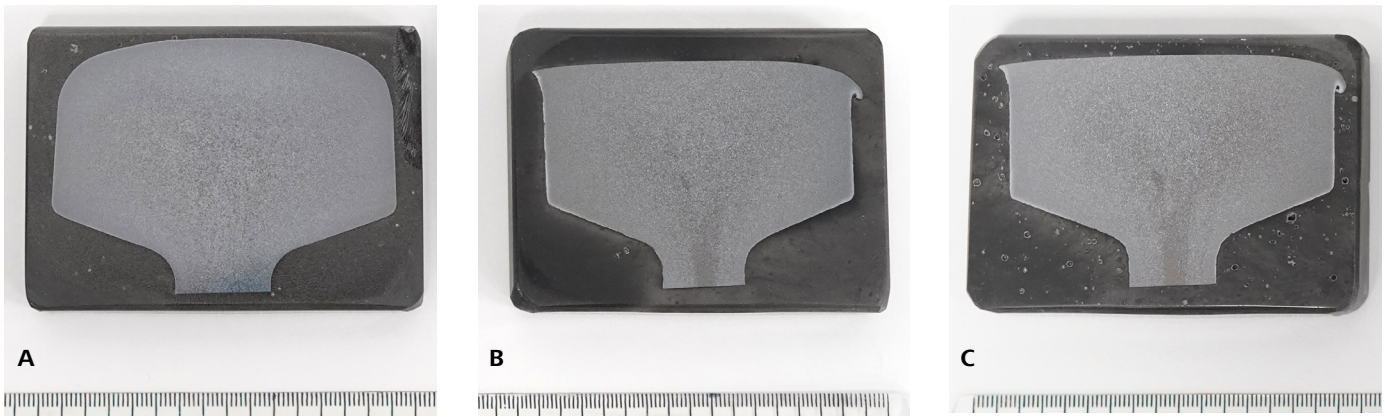

Figure 2 *Large cross-sections of the heads of rail track samples – A (2017), B (1940s-1950s) and C (1928-1932) respectively. Samples courtesy of Nene Valley Heritage Railway*

Light Microscopy

A detailed examination of Samples A-C was carried out using a ZEISS Axio Imager Z2.m utilising multiple contrast methods. The use of etchants and varying contrast modes in light microscopy yields much useful information on the grain structure, precipitates and impurities, variations in texture, corrosion and decarburisation. The microstructure was inspected in various regions, including at the surfaces. Where present, damaged regions were examined in detail.

Figure 3 shows that Sample A (2017) was primarily a pearlitic-martensitic steel. Examination of the near-surface regions on the underside of the head (where little or no wear should have occurred) showed the presence of white regions (in brightfield) along the grain boundaries – likely decarburization to a depth of 300-400 µm. A similar microstructure was present on the head of the on the head of the steel. Due to the lack of wear, this verified the rail had seen little or no use. Darkfield imaging highlighted these areas even more clearly, illustrating the value of multiple contrast modes in an examination by light microscopy. No significant non-metallic inclusions were visible, though this can be obscured by etching. Patchy and thin corrosion scale was present on the uppermost surface.

The microstructure of Sample B (1940s-50s), Figure 4, was substantially different. While still pearlitic there was some evidence of grain boundary segregation in the middle of the head. This is not present in the middle of the strut. The grain size was larger than that in the newer railway track (Sample A), indicative of different heat treatment and processing.

Sample A

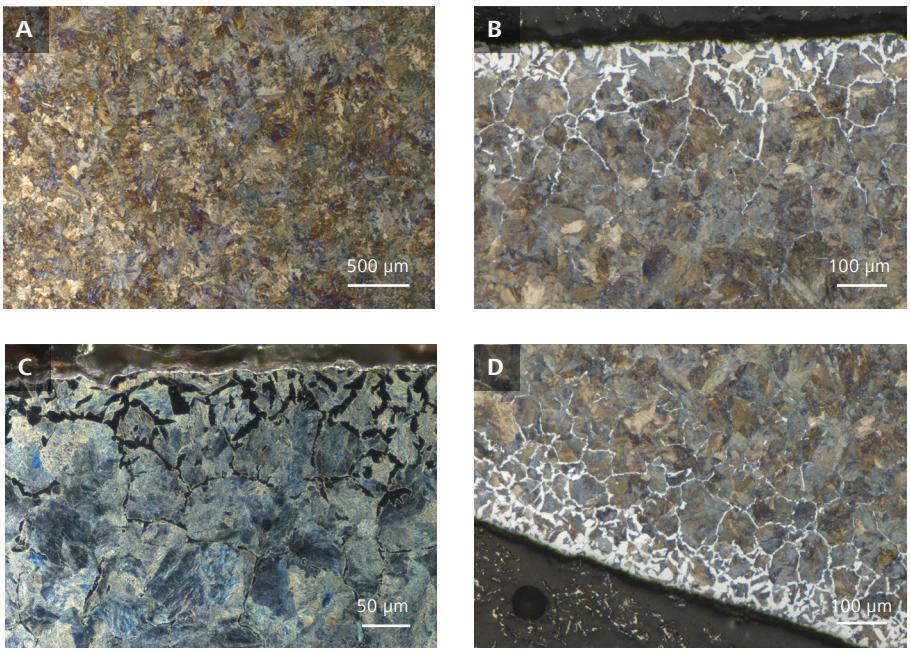

Figure 3 *Microstructure of Sample A (2017) – A) Center of the head, brightfield; B) Top of the head, brightfield; C) Top of the head, darkfield; D) Underside of the head, brightfield.*
Sample courtesy of Nene Valley Heritage Railway.

Several large non-metallic inclusions are visible in the both the head and the strut. In the strut, the sulfide inclusions are elongated in the vertical direction, due to the forging process. While these inclusions are also probably heavily elongated in the rolling direction, the cross-sections are taken perpendicular to the rolling direction and, as such, this elongation is not visible. This provides strong evidence for the age of the steel: while non-metallic inclusions are common to all steels, advances in steelmaking over the past 60 years have steadily reduced both the number and size of non-metallic inclusions typically found in steel. This high number of large inclusions is typical of an older grade.

The side of the strut shows heavy levels of decarburization, up to 620 µm deep. This is greater than Sample A (2017) and is indicative of a different steel composition and a different heat treatment/forging process. No decarburization was visible on the top surface: the microstructure here is almost identical to that in the middle of the head. It can be confirmed that a minimum of 600 µm of material wore away during service but considering the heavy damage on the right side, the damage was likely significantly deeper. Deformation and elongation of grains is visible in this area with cracking on the underside of the material. The whiter post-etching microstructure on the underside of the damaged region is likely due to the decarburized region remaining in place (though heavily deformed), local strain, and grain elongation.

Corrosion scale was visible on the upper surface and on the sides of the strut. In both cases, this was thicker than that observed on Sample A (2017). This scale was patchy, indicating it was not adherent or protective. This is typical of a standard oxide scale on steel.

Examining Sample C (1928-1932) confirms that the microstructure mid-head and mid-shaft is very similar to that observed in Sample B (1940s-50s), Figure 5. Segregation at the grain boundaries was present in the head only and the grains were larger than in Sample A (2017). There were high levels of non-metallic inclusions and decarburization on the side of the strut to a depth of approximately 600 µm. The top surface of the head showed identical microstructure to the middle of the head; any decarburized layer had long since been worn away. Corrosion scale was present on the surface.

The damage on the left side and right side of the head was more severe than in Sample B, with a greater volume of material bent over to a sharper angle. This was potentially indicative of greater length of service, or poorer resistance to deformation. Again, cracking was observed on the underside of the damaged curl, and the same grain elongation and preservation of some decarburized layer. Overall, the appearance of this rail was similar to that of Sample B (1940s-50s).

Sample B

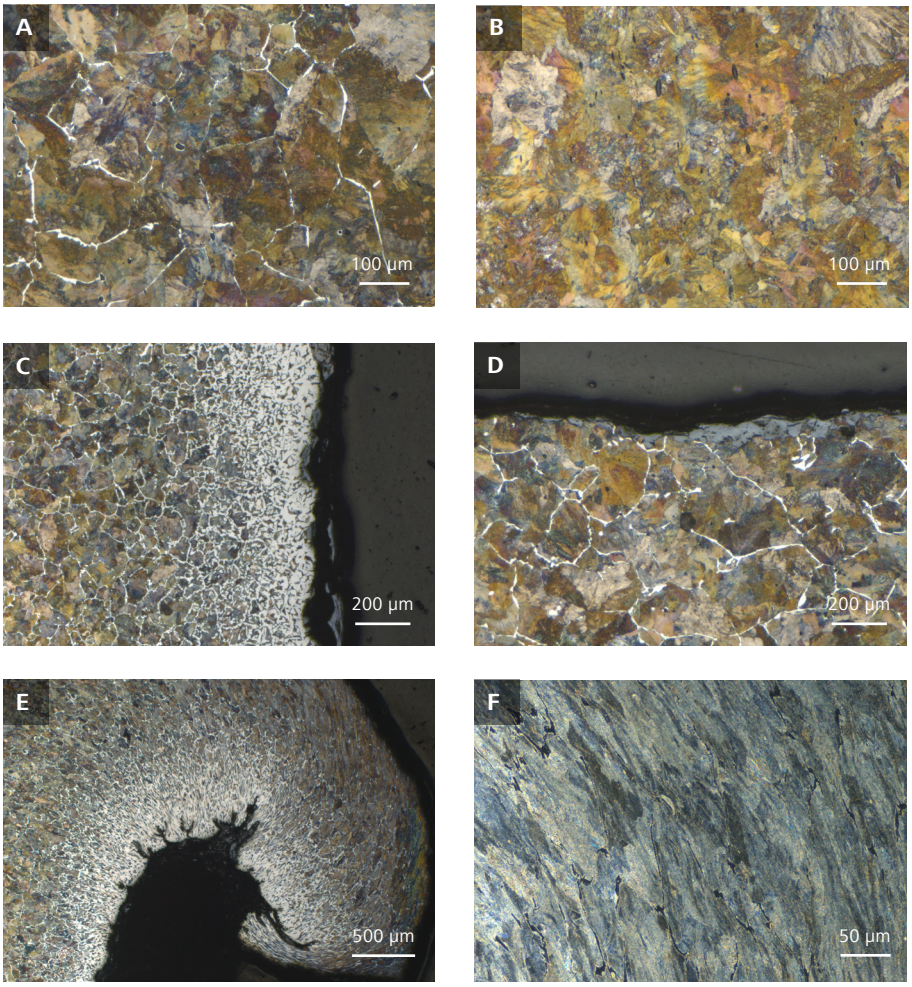

Figure 4 *Microstructure of Sample B (1940s-50s) – A) Center of head, brightfield; B) Center of strut, brightfield; C) Side of strut, brightfield; D) Top of head, brightfield; E) Damage to the rail on the right side, low magnification, brightfield; F) High magnification darkfield image of the damage.*
Sample courtesy of Nene Valley Heritage Railway.

Sample C

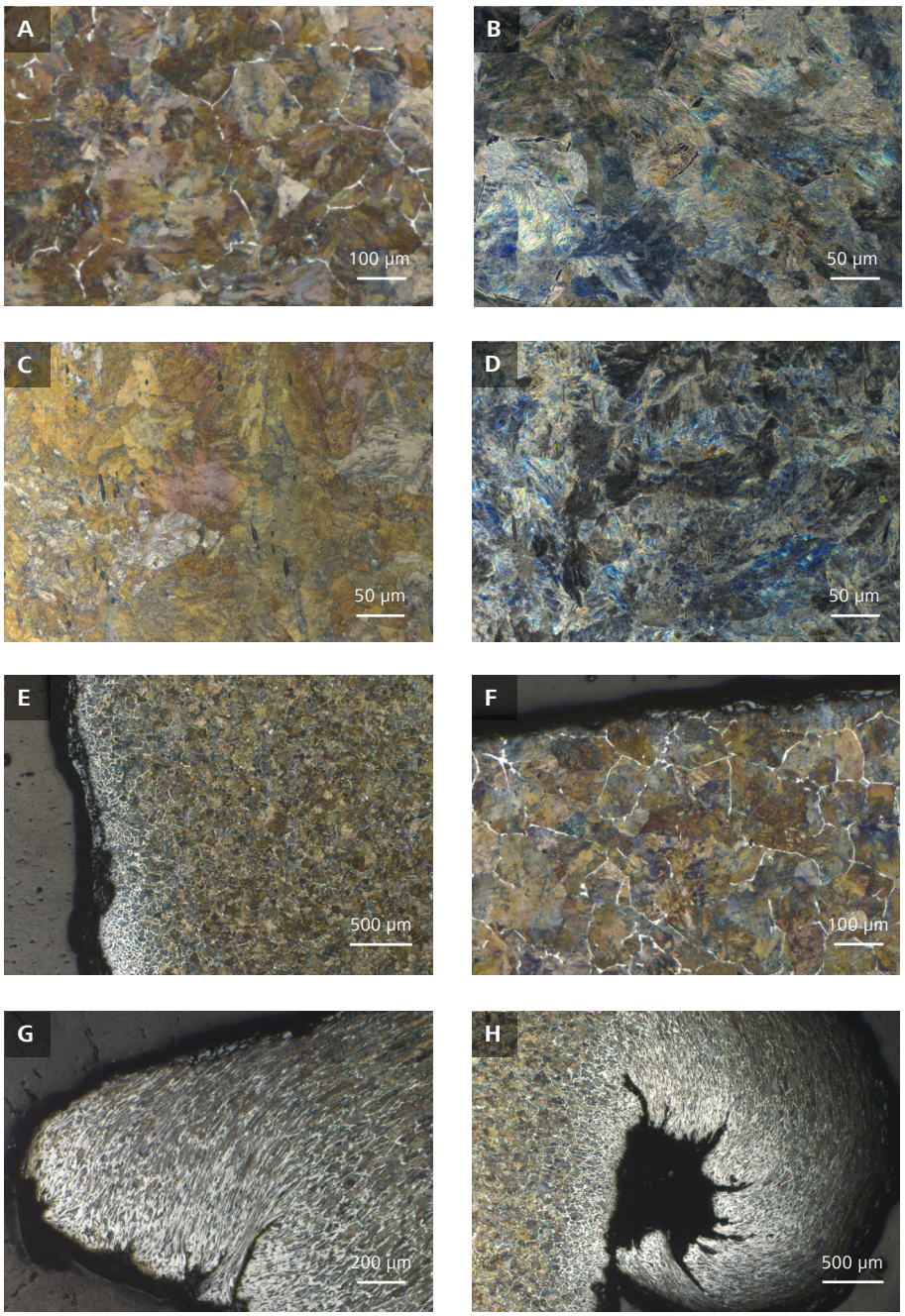

Figure 5 *Microstructure of Sample C (1928-1932) – A-B) Center of head, brightfield and darkfield; C-D) Center of strut, brightfield and darkfield; E) Side of strut, brightfield; F) Top of head, brightfield; G) Damage to the left side, brightfield; H) Damage to the right side, brightfield.*
Sample courtesy of Nene Valley Heritage Railway.

SEM of Inclusions

The large inclusions in the older steel (Sample B 1940s-50s) were examined using high resolution electron microscopy and energy-dispersive X-ray spectroscopy (EDS) to obtain further information on their type and distribution. These methods use different contrast modes and allow resolution of smaller features than light microscopy. Different detectors are sensitive to surface topography as well as local chemical composition with EDS permitting semi-quantitative analysis of constituents.

Example inclusions are shown in Figure 6. The structure is clearly pearlitic with visible cementite lamellae. The larger inclusion does not contain any oxygen and is primarily comprised of Mn and S, indicating it is a classic manganese sulfide inclusion. The smaller inclusion is primarily silicon oxide. X-rays emitted from this area also correspond to Mn and S (though weaker), indicating that this oxide inclusion may have a sulfide shell or there may be a sulfide inclusion below the oxide within the electron beam interaction volume.

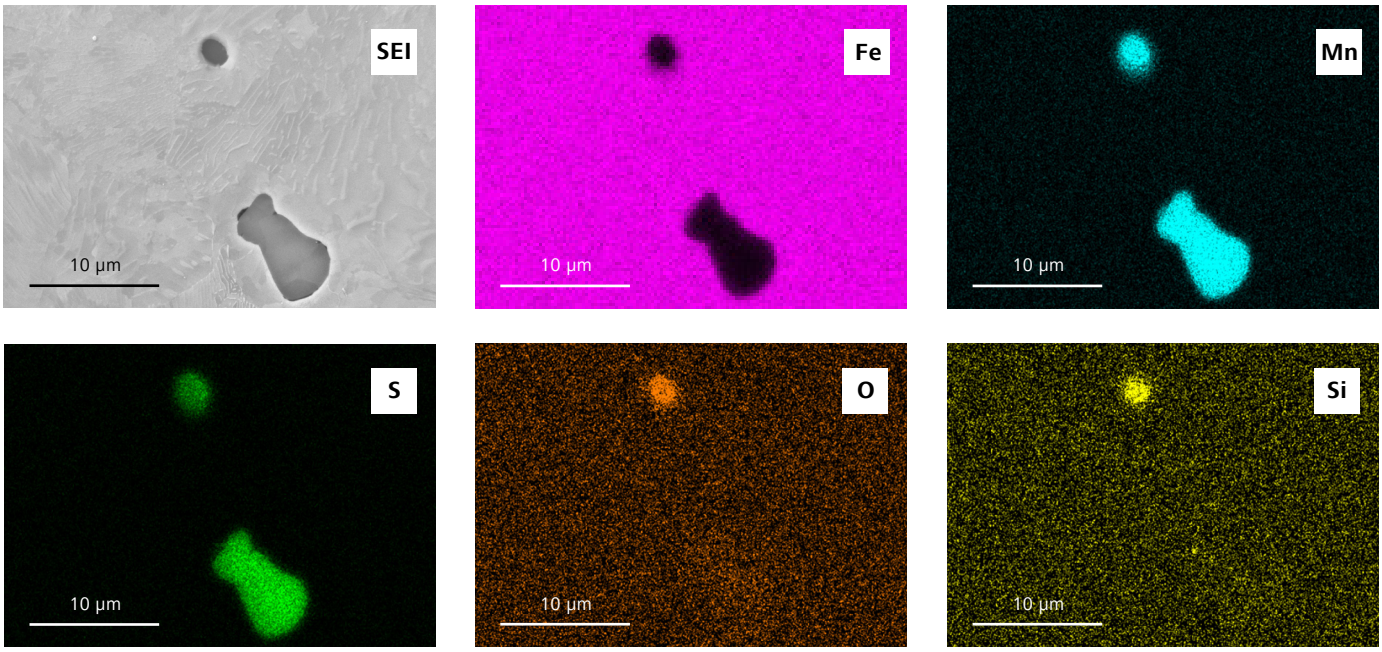

Figure 6 *Secondary electron image and EDS map of inclusions in Sample B (1940s-50s). Sample courtesy of Nene Valley Heritage Railway.*

Correlated Raman-SEM of corrosion scale – RISE imaging

All three samples of steel had clear layers of corrosion scale on the surface, from atmospheric exposure and service over the years. This is visible in cross-section both under light and electron microscopy as highlighted in Figures 3-5. Differentiating the corrosion scale layers was difficult by employing light microscopy, SEM and EDS due to the similarities in composition between the various iron oxides such as magnetite, hematite and goethite. These are composed of Fe, O and H. In addition, the relatively high interaction volume of the electron beam with the sample impedes examination of further details.

Raman spectroscopy—a technique that uses the interaction of photons with matter—provides information on molecular vibrations, thus is able to differentiate various iron oxides based on their molecular composition.

Using an excitation laser coupled with a confocal microscope, Raman spectra can be obtained from all points of the image with resolution in the sub-micron range. These Raman spectra are characteristic of organic and inorganic materials and allow the differentiation of materials with similar compositions but very different structures. The combination of Raman imaging and scanning electron microscopy (RISE microscopy) allows for high resolution structural analysis and a direct link of these structures to their chemical/molecular composition[3] (https://blogs.zeiss.com/microscopy/en/rise-microscopy/).

The smaller unetched cross-sections of Sample A (2017) and Sample B (1940s-50s) were loaded into a ZEISS Sigma 300 RISE microscope where the optimized geometries in the vacuum chamber combined with adapted beam path of a confocal Raman microscope and spectrograph (WITec) mean both techniques are easily integrated in a single microscope. This allows for both high resolution SEM imaging at variable pressure as well as confocal Raman measurements of non-metallic phases. The sample is automatically transferred between the two microscopes without leaving the SEM vacuum chamber, leading to a rapid workflow with fast, precise Raman analytics and correlation between between information from EM (e.g., secondary electron imaging, backscattered electron imaging, EBSD, EDS) and information from Raman spectra (compositional and structural maps). The focus of this area of study was the corrosion scale on the heads of Sample A and Sample B.

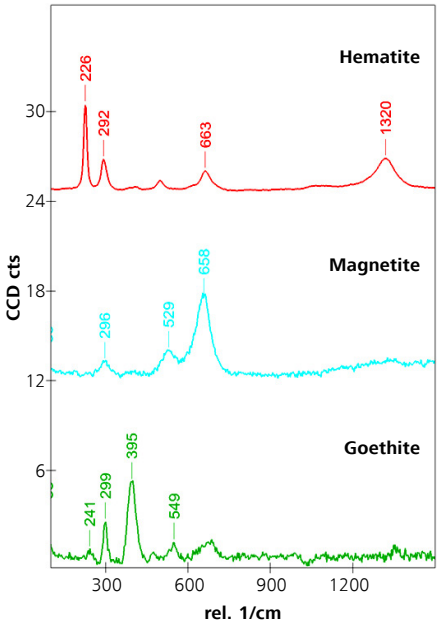

Figure 7 *Raman spectra of all the major constituents of corrosion scale on Samples A and B.*

For Raman imaging, the confocal Raman microscope was equipped with a 532 nm excitation laser and a 100x (NA=0.75) ZEISS vacuum objective. The spectroscopy package used for these measurements consists of a UHTS 300 VIS spectrograph with a focal length of 300 mm and a 600 g/mm, BLZ = 500 nm grating and a Newton CCD camera. The system used WITec Control FIVE for system control and WITec Project FIVE (Plus) for analysis, correlating with ZEISS SmartSEM.

From 2D arrays of Raman spectra acquired from both cross-sections, the Raman spectra of the relevant constituents of the corrosion scale on the track head were evaluated. Secondary electron images and standard white light micrographs were also taken of these regions, with corresponding EDS compositional maps. Combining all this information with the TrueMatch spectral search engine and using the RRUFF database of Raman spectra, the scale constituents were identified as the iron oxides hematite Fe_2O_3, magnetite Fe_3O_4, and the iron oxyhydroxide goethite FeO(OH). The spectra are shown in Figure 7. The steel is metallic and therefore does not generate a relevant Raman spectrum.

Combining both Raman data and EDS data, it was possible to get a better overall picture of the corrosion of each material. For Sample A (Figure 8), the corrosion scale on the head was primarily not sub-surface and consisted principally of goethite and magnetite, with some hematite. There was no correlation between distance from the steel and the scale formed, save that there was more goethite than hematite and magnetite. These iron compounds were only differentiable by Raman spectroscopy, due to the very similar levels of oxygen in the corrosion scale and the interaction volume of the electron beam.

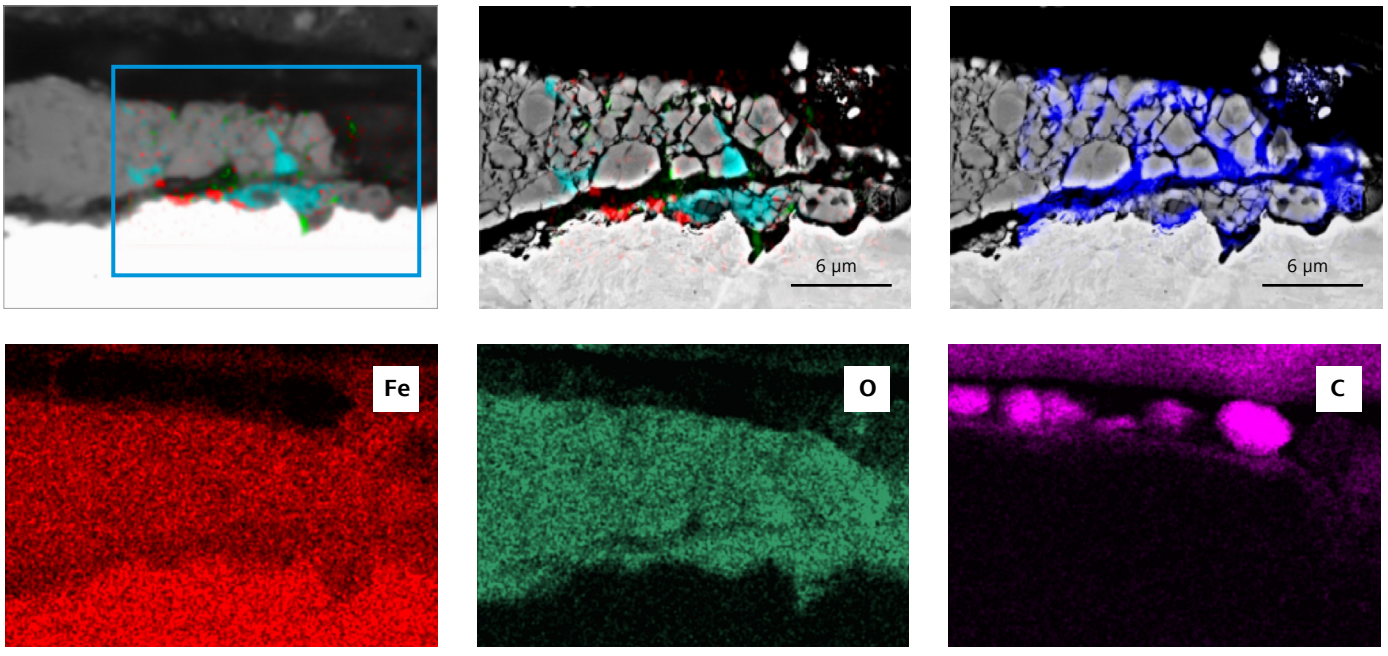

Figure 8 *Raman maps of corrosion scale on Sample A (2017), overlaid onto light micrograph and scanning electron micrograph. Red = hematite, Light blue = magnetite, green = goethite. An overlaid map of carbon distribution (dark blue) is also provided. EDS spectra of this region are shown. Sample courtesy of Nene Valley Heritage Railway.*

The scale was porous, as evidenced by high levels of carbon between parts of the scale, corresponding to metallographic mounting resin. This corrosion is likely a function of exposure of the fine-grained decarburized surface to the general atmosphere with intermittent wetting (weather).

For Sample B (1940s-50s), the corrosion behavior was completely different, Figure 9. No hematite was observed sub-surface, the scale consisted of magnetite close to the surface of the head and goethite further away. This gradient is a function of oxygen diffusion through the scale with magnetite (forming in a lower oxygen environment (with a lower oxidation state of iron). The hydrated oxide goethite is again a function of exposure to the general atmosphere plus plus weather events. Once again, these oxides were not easily differentiable by EDS alone.

The scale was less porous but penetrated deeper below the substrate (up to 30 µm) likely due to the larger grains and non-decarburized structure in this region. This is completely different corrosion behavior to that observed in the 2017 trail track. The localized corrosion on the already-worn region forms regions which themselves are less resistant to further wear.

Summary

The microstructure of the steel used for railway track has evolved over time as advances in steelmaking and studies of the correlation between composition, heat treatment and forging process have led to improved performance. The inclusion content has decreased, the grain size and microstructure have changed, all of which contribute to a change in corrosion mechanism and differences in performance under wear and other damage mechanisms.

To fully understand the steel performance and its dependence on the microstructure, light microscopy, scanning electron microscopy, EDS and Raman microscopy can be seamlessly combined to produce a connected and informative data set. This covers aspects as diverse as microstructural variation, damage incurred during service/storage and detailed insight into the corrosion mechanism.

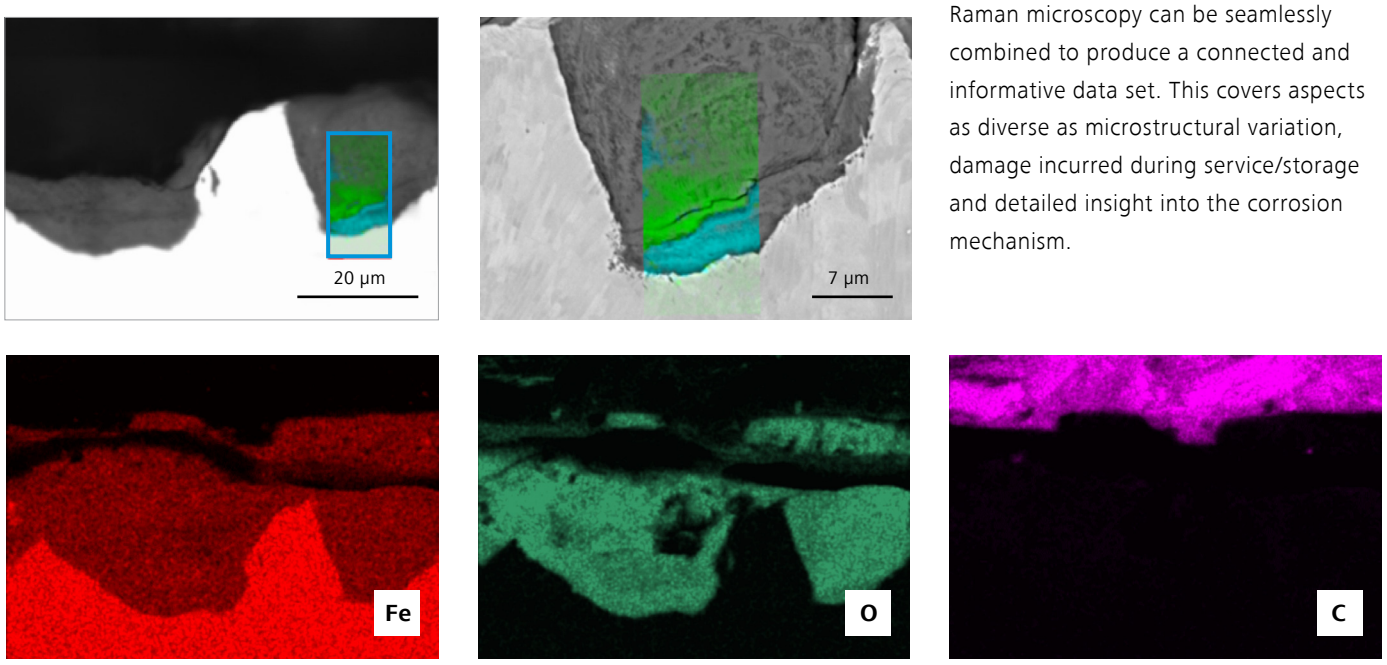

Figure 9 *Raman maps of corrosion scale on Sample B (1940s-50s), overlaid onto light micrograph and scanning electron micrograph. Red = hematite, Light blue = magnetite, green = goethite. EDS spectra of the wider region are shown. Sample courtesy of Nene Valley Heritage Railway.*

References

[1] Oxford Economics Report 2018 "The Economic Contribution of UK Rail," www.oxfordeconomics.com

[2] International Railway Journal October 2015 (Sue Morant) "Next-generation super-premium rail steels hit the tracks," https://www.railjournal.com/in_depth/next-generation-super-premium-rail-steels-hit-the-tracks

[3] ZEISS Blog "Witec's RISE Microscopy Now Available with ZEISS Sigma 300 Scanning Electron Microscope" https://blogs.zeiss.com/microscopy/en/rise-microscopy/

Carl Zeiss Microscopy GmbH
07745 Jena, Germany
microscopy@zeiss.com
www.zeiss.com/metals